Nano Research

Open Access

Research Article

Organic ion building blocks-assembled carboxyl ionic single crystals for ultra-selective and ultrafast uranium extraction

Jing He[1,2], Jia Chen[1,2] ✉, Yongxing Sun[1], Zijie Li[3], Huifeng Liu[1], Juanjuan Wang[1], Weiqun Shi[4] ✉, and Hongdeng Qiu[1,2,5] ✉

[1] *Key Laboratory for Natural Medicine of Gansu Province, Lanzhou Institute of Chemical Physics, Chinese Academy of Sciences, Lanzhou 730000, China*
[2] *University of Chinese Academy of Sciences, Beijing 100049, China*
[3] *Laboratory of Nuclear Energy Chemistry, Institute of High Energy Physics, Chinese Academy of Sciences, Beijing 100049, China*
[4] *Institute of Nuclear Fuel Cycle and Materials, School of Mechanical Engineering, Shanghai Jiao Tong University, Shanghai 200240, China*
[5] *Key Laboratory of Rare Earths, Ganjiang Innovation Academy, Chinese Academy of Sciences, Ganzhou 341000, China*

Cite this article: *Nano Research*, **2025**, *18*, 94907856. https://doi.org/10.26599/NR.2025.94907856

ABSTRACT: Uranium extraction from seawater (UES) is crucial for reducing nuclear fuel supply pressure and promoting the comprehensive utilization of marine resources. The successful implementations of UES engineering critically rely on the highly efficient sorbent materials with exceptional performance in binding uranyl ions. Herein, a universal and facile "organic ion building blocks self-assembly" strategy is established to realize a first class of carboxyl functionalized ionic single crystals, named BPTC-BPY-*R* (*R* = 1–6, the *R* corresponds to alkyl chain length modifier, e.g., *R* = 1 corresponds to iodomethane derivatives, *R* = 2 corresponds to bromoethane derivatives, etc.), derived from rationally designed viologen-derivatives with different alkyl chain lengths and polycarboxylic acid. This strategy effectively exploits the organic ion building block properties to achieve U(VI) adsorption based on the synergistic effects of anions (ligand interaction) and cations (electrostatic interaction). Notably, attributed to the special crystal stacking mode and higher specific surface area, the resulting BPTC-BPY-3 not only achieves ultrahigh selectivity for U(VI) adsorption with a partition coefficient of 3.998 × 10^6 mL/g, but also possesses an ultrafast U(VI) adsorption kinetics and an uptake capacity of 686.8 mg/g within 2 min. More importantly, it realizes a U(VI) uptake capacity of 7.41 mg/g from natural seawater in 20 days. The designed material with ultra-selectivity, high capacity, ultrafast kinetics, and good recyclability exhibits a great promise for efficient U(VI) extraction from seawater.

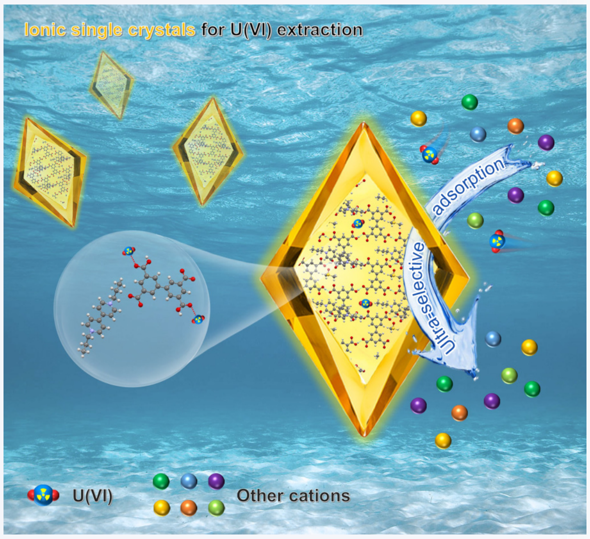

KEYWORDS: ionic self-assembly, single crystal, uranium extraction, organic ion building block, chain length tuning

1 Introduction

Uranium extraction from seawater (UES) has gained recognition as one of the seven major chemical separations with the potential to revolutionize the world [1, 2]. With 4.5 billion tons of U(VI) widely distributed in seawater, the reserves are at least 1000 times greater than those found on all known landmasses [3]. However, UES presents significant long-term engineering challenges due to the predominant form of uranium in seawater, $[(UO_2(CO_3)_3]^{4-}$, which is present in an ultra-low concentration of approximately 3.3 ppb [4, 5]. Additionally, the high salt concentration and prolonged exposure to seawater pose further complications, as other ions in the seawater can greatly impact the materials used for UES [6]. Consequently, the development of efficient and cost-effective materials for extracting uranium from seawater becomes imperative [7–10].

Effective control of adsorption and accurate separation of U(VI)

Received: March 24, 2025; **Revised:** June 13, 2025
Accepted: July 31, 2025

✉Address correspondence to Jia Chen, jiachen@licp.cas.cn; Weiqun Shi, shiwq@sjtu.edu.cn; Hongdeng Qiu, hdqiu@licp.cas.cn

is crucial in this process, which is achieved by considering the coordination environment of U(VI). Hitherto, researchers have explored various U(VI) adsorbents, encompassing inorganic materials [11–13], polymers [14, 15], biomaterials [16], and nanomaterials [17–19]. To facilitate practical implementation in seawater, macroscopic adsorbents, such as fibers [20, 21], resins [22], and hydrogels [23–25], have been specifically designed. However, these adsorbents are typically electrically neutral and rely on the functional groups (e.g., amidoxime groups, sulfonate groups, and carboxyl groups) therein for coordination [26], and their selectivity for U(VI) is limited, which is further exacerbated by interference from vanadyl ions [27, 28]. A further critical challenge lies in the adsorption capacity of existing materials, which often underutilize interfacial sites, resulting in low U(VI) uptake and slow adsorption rates [29, 30]. Studies have demonstrated that introducing charged functional groups into the organic ligand of the adsorbent can significantly enhance selectivity and adsorption rates [31–34]. The studies have inspired our interest to simultaneously introduce organic anion-cation building blocks and multiple adsorption sites on the materials [35–38], aiming to efficiently improve the selectivity and adsorption capacity through the synergistic effect of combining electrostatic interactions and coordination interactions.

Herein, we firstly put forward a universal and facile strategy for synthesizing a novel class of carboxyl ionic single crystals with unique network structures, named BPTC-BPY-*R* (*R* = 1–6, the *R* corresponds to alkyl chain length modifier, e.g., *R* = 1 corresponds to iodomethane derivatives, *R* = 2 corresponds to bromoethane derivatives, etc.), which were assembled by organic cation building block (dialkyl bipyridine dihalide, BPY-R) and organic anion building block (biphenyl-3,3',5,5'-tetracarboxylic acid, H_4BPTC). Notably, by modulating the alkyl chain length in BPY-R (viologen-derived), these materials were successfully formed at room temperature through electrostatic interactions. In this case, the weak acidity of the carboxyl group in H_4BPTC was skillfully improved by the addition of $NH_3{\cdot}H_2O$. The exceptional U(VI) adsorption properties of the material were further confirmed through the systematic variation of experimental parameters, including adsorbent dosage, pH, temperature, as well as analysis of adsorption isotherms, kinetics, thermodynamics, selective adsorption, and regeneration experiments for U(VI). We also examined the adsorption capacity of the material in natural seawater and verified the synergistic adsorption mechanisms by integrating theoretical calculations with experimental investigations.

2 Results and discussion

2.1 Design, synthesis, and characterizations of BPTC-BPY

Firstly, a series of network ionic single crystal materials, BPTC-BPY-*R* (*R* = 1–6), were facilely obtained by the ionic self-assembly of H_4BPTC and BPY-R at room temperature, as depicted in Fig. 1(a). The exact structures of these single crystals were analyzed by single-crystal X-ray diffraction (SC-XRD) (Tables S1–S6 in the Electronic Supplementary Material (ESM)). SC-XRD analysis indicates that the ionic single crystals BPTC-BPY-*R* (*R* = 1–6) in this work have an organic anion-cation building block ratio of 1:1 (as shown by the asymmetric unit of BPTC-BPY-*R* in Fig. S1 in the ESM), where each ionic single crystal was formed by multiple ionic bonds with a bond length of 2.74–3.81 Å (Fig. 1(b)), which in turn effectively formed a unique three-dimensional structure. While these ionic single crystals exhibit a variety of typical stacking modes, including inserted-stacking, mixed-stacking, and segregated-stacking, as shown in Fig. S2 in the ESM. In the inserted-stacking mode, the organic anion-cation building blocks alternately stack along their face-to-face stacking directions, represented by BPTC-BPY-1 and BPTC-BPY-2. In the mixed-stacking mode, some organic ion building blocks can be stacked separately in adjacent layers through the separation stacking mode, and additional organic ion building blocks can be inserted into the separation stacking layer through electrostatic action under the separation stacking layer, represented by BPTC-BPY-4. Meanwhile, in a segregated-stacking mode, organic anion-cation building blocks are stacked in adjacent layers, respectively, and the layers are combined by electrostatic interaction, typical examples being BPTC-BPY-3, BPTC-BPY-5, and BPTC-BPY-6. Different stacking modes are expected to influence the physicochemical properties of BPTC-BPY-*R* and their corresponding U(VI) adsorption performance.

Upon comparing the experimental and simulated powder XRD (PXRD) patterns, a remarkable concurrence can be observed. For BPTC-BPY-2, BPTC-BPY-3, and BPTC-BPY-4, the experimental PXRD patterns exhibit a striking resemblance to the simulated PXRD patterns, showcasing diffraction peaks of comparable intensities at identical positions. This congruence strongly suggests that the samples possess excellent crystallinity and phase purity. Unfortunately, BPTC-BPY-1, BPTC-BPY-5, and BPTC-BPY-6 are prone to weathering due to the unstable exposure of single crystals in air, so the experimental PXRD patterns cannot completely overlap with the simulated PXRD patterns, but do not affect the performance of single crystals and adsorption experiments, as depicted in Figs. 2(a)–2(f). The chemical stability of BPTC-BPY-*R* was evaluated with BPTC-BPY-4 as a representative. After exposure to various chemical environments at room temperature for 24 h, BPTC-BPY-4 maintained its crystal structure in various organic solvents, which means excellent chemical stability (Fig. S3 in the ESM). When dispersed in aqueous solutions with different pH ranges, the intensity of the PXRD pattern of BPTC-BPY-4 remained relatively stable from pH = 3–7. Therefore, this material has acid resistance in a certain range. The morphology of BPTC-BPY-*R* was subsequently characterized by optical microscopy, as shown in Figs. 2(g)–2(l). The synthesized BPTC-BPY-*R* appeared as bulk or needle-shaped transparent crystals, and the photographs clearly illustrate its angular shape and dimensions ranging from 0.1 to 1.7 mm. For example, BPTC-BPY-3 manifested as a bulk, parallel prismatic, yellow transparent crystal with a size of about 100 μm (Fig. 2(i)). Thermogravimetric (TG) analysis of BPTC-BPY-*R* demonstrated their similar and good thermal stabilities. It was observed that BPTC-BPY-*R* maintained its significant weight until 270 °C (small mass loss due to solvent), followed by a gradual weight reduction due to the combustion of the ionic single crystal frame in air (Fig. 2(m)).

The characteristic functional groups of single-crystal products, as well as the corresponding raw materials, were investigated using Fourier transform infrared (FT-IR) spectroscopy (Fig. 2(n) and Fig. S4 in the ESM). The characteristic peaks at 1703 and 1637 cm^{-1} corresponded to the stretch vibration of C=O and C–N, respectively, in H_4BPTC and BPY-R. Subsequently, FT-IR spectra of the synthesized BPTC-BPY-*R* illustrate the presence of C=O (~ 1713 cm^{-1}) and C–N (~ 1636 cm^{-1}). In addition, a wide peak at 3000 cm^{-1} corresponds to the C–H stretch vibration of the alkyl

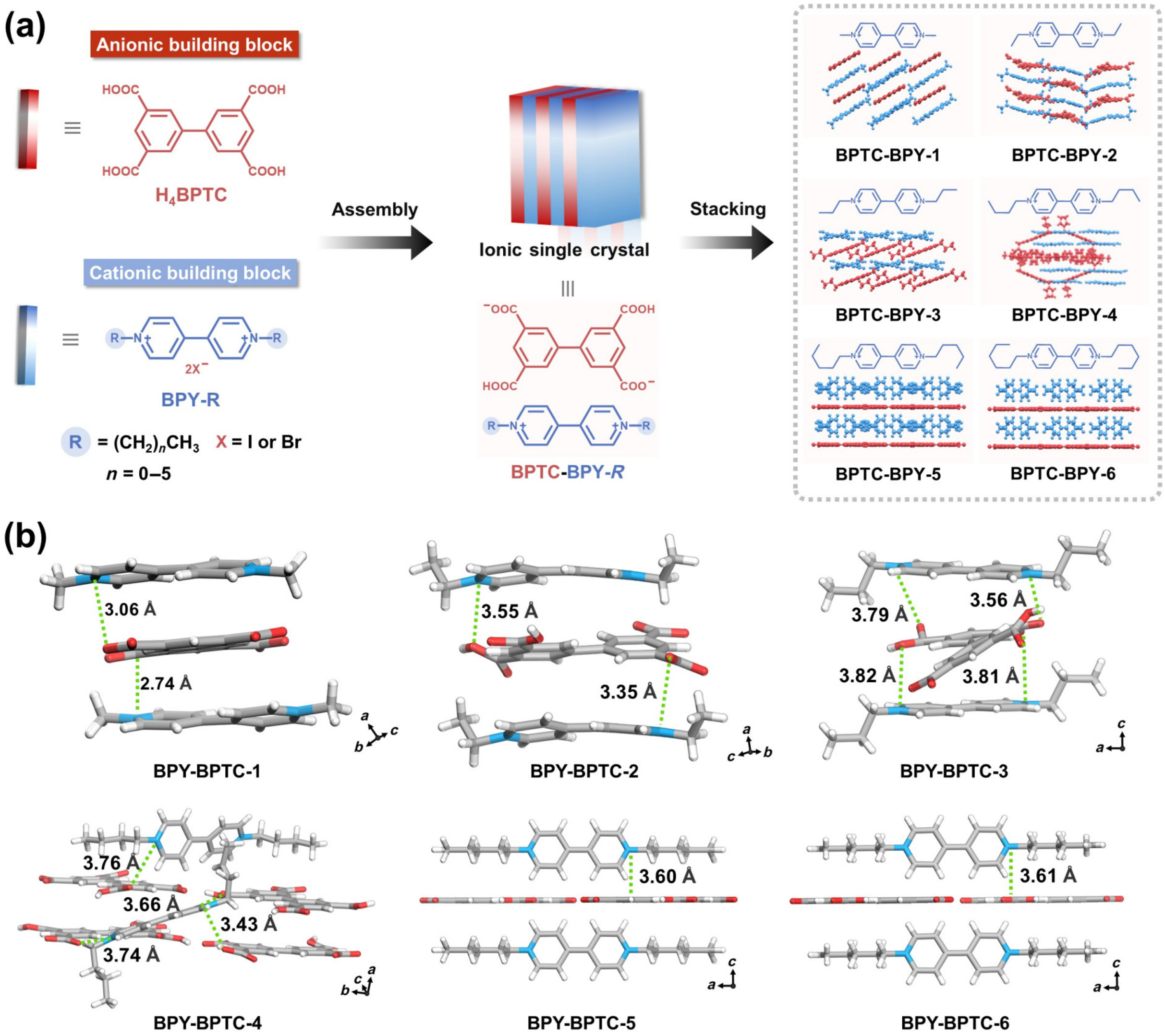

Figure 1 (a) Synthesis of ionic single crystals of BPTC-BPY-*R* and (b) the ionic bonds between H_4BPTC and BPY-R.

chain. These results demonstrate the successful synthesis of the ionic single crystal materials. The specific surface areas and pore size characteristics of BPTC-BPY-*R* were investigated through CO_2 adsorption–desorption. The specific surface area of BPTC-BPY-*R* was calculated to be 8.3, 16.3, 67.1, 33.0, 58.8, and 4.2 m^2/g (Fig. 2(o) and Fig. S5 in the ESM). Meanwhile, the pore size distributions indicate that the materials have a complex micropore structure (Fig. S6 in the ESM). This intricate pore architecture facilitates the diffusion of seawater within BPTC-BPY-*R*, thereby enhancing ion transport and augmenting the U(VI) adsorption capacity of the material. Then, we investigated the hydrophilic properties of BPTC-BPY-*R* using water contact angle measurements. The results revealed that an increase in hydrophobicity from 9.7° to 57.9° with increasing alkyl chain length in the anionic ligands (Fig. 2(p) and Figs. S7–S12 in the ESM). These findings indicate the strong hydrophilicity of these materials, enabling effective U(VI) adsorption.

2.2 Adsorption performance and influencing factors for U(VI)

The adsorption performance is significantly correlated with the pH of the solution, as it affects both the chemical form of U(VI) and the surface charge of the adsorbent. Consequently, the effect of alkyl chain length and pH on the uranium extraction was investigated by evaluating the adsorption capacity and zeta potential of BPTC-BPY-*R*. Compared to other ionic single crystal materials, U(VI) adsorption capacity analysis revealed that BPTC-BPY-3 exhibited the highest uranium adsorption capacity of 405.2 mg/g in uranyl nitrate aqueous solution at pH = 6 (Fig. 3(a)). This may be attributed to the special crystal stacking mode and larger specific surface area of BPTC-BPY-3, which was able to expose more adsorption sites, allowing more U(VI) species to be adsorbed into the structure [39]. Additionally, the isoelectric point of BPTC-BPY-3 was 2.9 (Fig. 3(b)). When the pH value was less than 2.9, the positively charged uranium groups experienced repulsion from the positively charged BPTC-BPY-3 surface, resulting in a decreased adsorption capacity for uranium. As the pH increased, the surface of BPTC-BPY-3 became negatively charged, leading to a gradual increase in adsorption capacity. At this point, the adsorption of U(VI) may be attributed to the electrostatic attraction, which makes uranium closer to the active site, which not only improves the kinetics but also improves the utilization rate of functional groups. Starting from pH = 4, various forms of uranium hydrolysis occurred, with the dominant species being UO_2^{2+} (Fig. 3(c)).

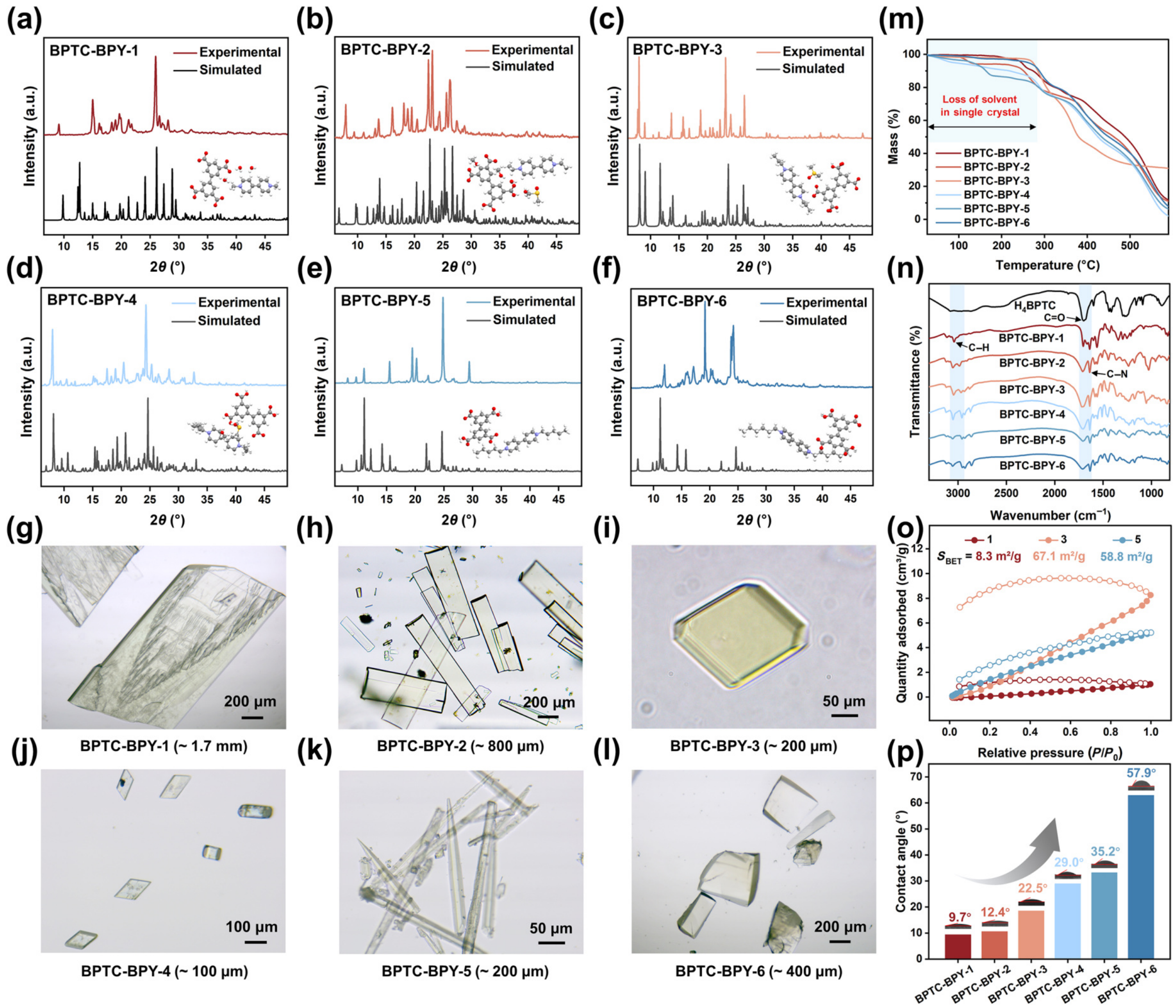

Figure 2 Morphological and structural characterizations of ionic single crystal BPTC-BPY-*R* (*R* = 1–6). ((a)–(f)) Experimental and simulated PXRD patterns. ((g)–(l)) Optical microscopy. (m) Thermo gravimetric analysis (TGA) plot. (n) FT-IR spectra of H_4BPTC and BPTC-BPY-*R*. (o) CO_2 adsorption–desorption profile of BPTC-BPY-*R* (*R* = 1, 3, and 5) and (p) water contact angle.

Whereas, when the pH exceeded 6, the adsorption capacity gradually decreased. This may be attributed to the continuous deprotonation of the adsorbent, resulting in an increased negative charge that hinders the adsorption of negatively charged U(VI) species in the material. Thus, pH = 6 was chosen for subsequent adsorption experiments. Furthermore, the solid–liquid ratio in the adsorption solution was investigated. The removal rate of uranium with the BPTC-BPY-3 concentration increased from 0.1 to 0.5 g/L, reaching a plateau at 0.4 g/L (Fig. S13 in the ESM). However, with the increase in remove rate value, the adsorption capacity decreases. For ensuring both high adsorption capacity and removal rate, a solid–liquid ratio of 0.4 g/L was used in the subsequent experiments.

2.3 Adsorption isotherms, kinetics, and thermodynamics studies

To elucidate the effect of the initial U(VI) concentration on the adsorption of BPTC-BPY-*R*, the adsorption isotherms of 50–600 ppm U(VI)-loaded solution were plotted. The results showed that the maximum adsorption capacities of BPTC-BPY-*R* (*R* = 1–6) were 241.3, 275.0, 686.8, 293.3, 147.4, and 39.4 mg/g, respectively, among which BPTC-BPY-3 showed outstanding adsorption capacity (Fig. 3(d)). Therefore, BPTC-BPY-3 was chosen as the representative of ionic single crystals for subsequent U(VI) adsorption experiments. To delve deeper into the interaction mechanism between the adsorbent material and U(VI), the adsorption experimental data were fitted with the Langmuir and Freundlich adsorption isotherm models (Fig. 3(e) and Table S7 in the ESM). The correlation coefficient (R^2) obtained from the Langmuir model fitted to the experimental data was 0.99, while the R^2 of the Freundlich model was 0.92. The above results showed that the adsorption of U(VI) by BPTC-BPY-3 was consistent with the Langmuir isotherm model, with the active adsorption sites uniformly distributed on the surface of the material, and the adsorption of U(VI) was monolayer adsorption.

Adsorption time is one of the important parameters affecting the adsorption efficiency of U(VI) by the adsorbent. Within 1 min, the adsorption capacity of BPTC-BPY-3 on U(VI) increased sharply, reaching equilibrium within 2 min. To further investigate the kinetics of U(VI) adsorption by the material, the above adsorption experimental data were fitted by using the proposed first-order kinetic equation and the proposed second-order kinetic equation (Fig. 3(f) and Table S8 in the ESM). The R^2 obtained by fitting the proposed first-order kinetic equation to the experimental kinetic data is 0.917, and the proposed second-order kinetic equation fits

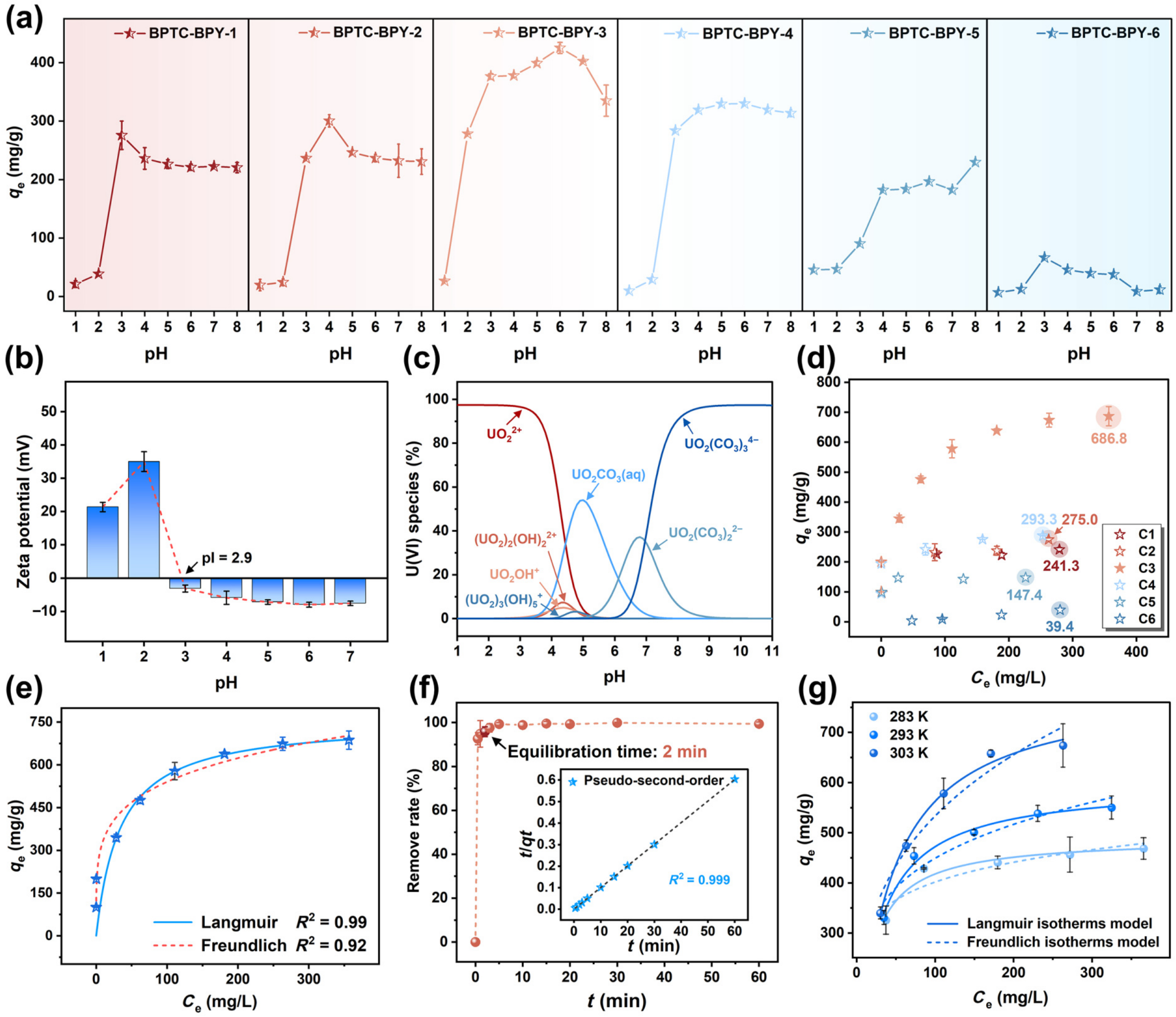

Figure 3 U(VI) adsorption performance. (a) Optimal pH for U(VI) adsorption of BPTC-BPY-*R* (*R* = 1–6). (b) Values of zeta potentials at different initial pH values of BPTC-BPY-3. (c) Existing forms of uranium at different pH conditions. (d) Adsorption isotherms of BPTC-BPY-*R* (*R* = 1–6). (e) The Langmuir and Freundlich isotherm models of BPTC-BPY-3. (f) Effect of contact time on the adsorption process of U(VI) and linear quasi-secondary kinetic modeling of BPTC-BPY-3. (g) Effect of temperature of BPTC-BPY-3.

the experimental kinetic data better, with a R^2 as high as 0.999 and a calculated adsorption capacity of 199.75 mg/g, which was close to the experimental value. That is to say, the adsorption of U(VI) aligns more closely with the proposed second-order kinetic equation, indicating that the chemical adsorption predominantly governs the adsorption of U(VI) by the material.

Meanwhile, the effect of BPTC-BPY-3 on the adsorption capacity of U(VI) at different temperatures (283, 293, and 303 K) was investigated (Fig. 3(g) and Fig. S14 in the ESM). Results indicated that higher temperatures enhanced U(VI) adsorption capacity, suggesting an endothermic nature of the adsorption process. Subsequently, the thermodynamic characteristics of the U(VI) adsorption process were investigated, and the thermodynamic parameters, enthalpy (H^0), entropy (S^0), and Gibbs free energy (G^0), were calculated according to the equations (Table S9 in the ESM). Analysis of the data reveals that the positive H^0 signifies an endothermic nature of the U(VI) adsorption process, while positive S^0 suggests that an increase in disorder at the solid–liquid interface during the process of U(VI) adsorption. Across various temperatures, the negative and decreasing G^0 with increasing temperature, indicates that the process of U(VI) adsorption by the material is spontaneous.

2.4 Practical application studies

While the majority of the uranium extraction studies reported are based on batch experiments [40, 41], the penetration experiments, which closely mirror practical applications, have been scarcely examined. The dynamic loading adsorption performance of BPTC-BPY-3 for a high initial concentration (50 ppm) of U(VI) using a penetration curve was evaluated (Fig. 4(a)). The experimental results, depicting the normalized uranium percentage at the outlet as a function of volume, were illustrated in Fig. 4(b). The fixed bed maintained a high removal efficiency of up to 30 mL, beyond which U(VI) began to penetrate the BPTC-BPY-3 fixed bed, with complete breakthrough occurring after 100 mL. These results underscore that the material has robust performance in practical applications.

To determine the recyclability of BPTC-BPY-3, an eluent containing sodium carbonate (1 M) and hydrogen peroxide (0.1 M) was used to elute uranium from the U(VI)-loaded adsorbent. In the

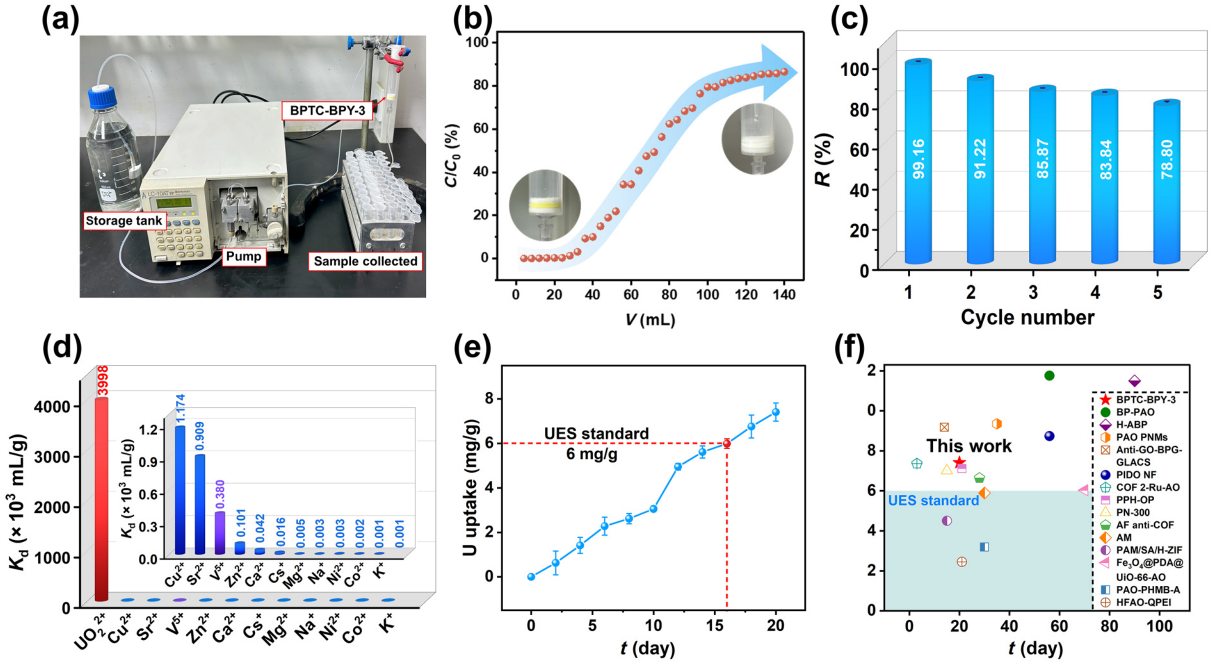

Figure 4 Practical adsorption performance of U(VI). (a) Penetration experimental setup. (b) Penetration curves of fixed-bed U(VI) adsorption. (c) Adsorption–desorption cycle of U(VI) in solution. (d) K_d of BPTC-BPY-3 for different cations. (e) The adsorption performance for U(VI) during 20 days with natural seawater. (f) Comparison of adsorption capacities against the duration of adsorption of uranium for some excellent adsorbents from natural seawater (references can be found in Table S10 in the ESM).

presence of carbonate and hydrogen peroxide, an extremely stable uranyl peroxycarbonate complex was formed, resulting in the elution of bound U(VI) from the adsorbent. The initial elution cycle achieved a remarkable elution efficiency of 99.16% (Fig. 4(c) and Fig. S15 in the ESM), which is crucial for the recovery of uranium resources from aqueous solutions. After four regeneration cycles, the material retained 78.80% of its initial adsorption capacity, demonstrating satisfactory reproducibility of the U(VI) adsorption rate and capacity, making it suitable for U(VI) adsorption experiments in natural seawater.

Given the high salt concentration in seawater, we explored the effect of NaCl concentration on U(VI) adsorption experiments. As the salt concentration increased from 0.2 to 1 M, BPTC-BPY-3 maintained a stable U(VI) adsorption capacity (Fig. S16 in the ESM), indicating robust performance in the high-salt environment. Another important factor that significantly affects the effectiveness of U(VI) adsorption is adsorption selectivity. Natural seawater contains various highly concentrated interfering ions coexisting with U(VI), which seriously impedes the adsorption of trace amounts of uranium. Hence, the selective adsorption of U(VI) amidst a mixture of interfering ions is essential for uranium extraction from seawater. The partition coefficient (K_d) was calculated to evaluate the affinity of uranium for the material. In general, materials with K_d values > 10^4 mL/g are considered good adsorbents for uranium recovery [42]. In the work, the calculated K_d value of BPTC-BPY-3 is about 3.998 × 10^6 mL/g, which is comparable to or superior to the excellent adsorbents reported so far in Refs. [43–45]. For other metal ions commonly found in seawater (including Na^+, K^+, V^{5+}, Zn^{2+}, Sr^{2+}, Cs^+, Cu^{2+}, Ni^{2+}, Ca^{2+}, Co^{2+}, and Mg^{2+}), the K_d values are less than 2 × 10^3 mL/g, highlighting the BPTC-BPY-3 is extremely selective for U(VI) (Fig. 4(d)). The excellent selectivity for U(VI) compared to other ions is attributed to the strong affinity between U(VI) and the functional groups anchored on the surface of the ionic single crystal. All these outstanding adsorption performance characteristics suggest that BPTC-BPY-3 can be used as a unique adsorbent for ultra-selective recovery of uranium from seawater.

Furthermore, the U(VI) adsorption performance of BPTC-BPY-3 in low-concentration simulated seawater was investigated. The adsorbent demonstrated significant adsorption efficacy on U(VI) in the 2–800 ppb range (Fig. S17(a) in the ESM). BPTC-BPY-3 was also applied to unspiked natural seawater from the Yellow Sea of China with an adsorption amount of BPTC-BPY-3 in 4 L, and the results are shown in Fig. 4(e). The adsorption capacity was determined to be an impressive 7.41 mg/g after 20 days of immersion in natural seawater. The detailed adsorption data for UES are shown in Table S10 in the ESM. This rapid recovery of U(VI) from natural seawater is comparable to some of the known excellent adsorbents (Fig. 4(f) and Table S11 in the ESM) [14, 43, 45–56]. Concurrently, the capture of trace U(VI) from spiked natural seawater was investigated (Fig. S17(b) in the ESM). U(VI) was spiked at 2, 4, and 8 ppm, respectively, and it was observed that the adsorption kinetics of BPTC-BPY-3 effectively reduced the U(VI) concentration from 8 to 6.66 ppm within 30 min, with proportional reductions at other concentrations. To verify the stability of the adsorbent in seawater for extended periods of time, we analyzed the changes in FT-IR spectra and scanning electron microscopy (SEM) image of BPTC-BPY-3 after 1, 7, and 14 days of adsorption of U(VI). After 14 days, FT-IR spectra showed that no significant changes in surface functional groups were observed, and characteristic peaks of U(VI) were still detectable (Fig. S18 in the ESM). In addition, the SEM images showed no significant changes in the sorbent surface (Fig. S19 in the ESM), indicating that the structure retains excellent stability even after prolonged exposure. These results indicate that the material can effectively adsorb trace amounts of uranium from natural seawater.

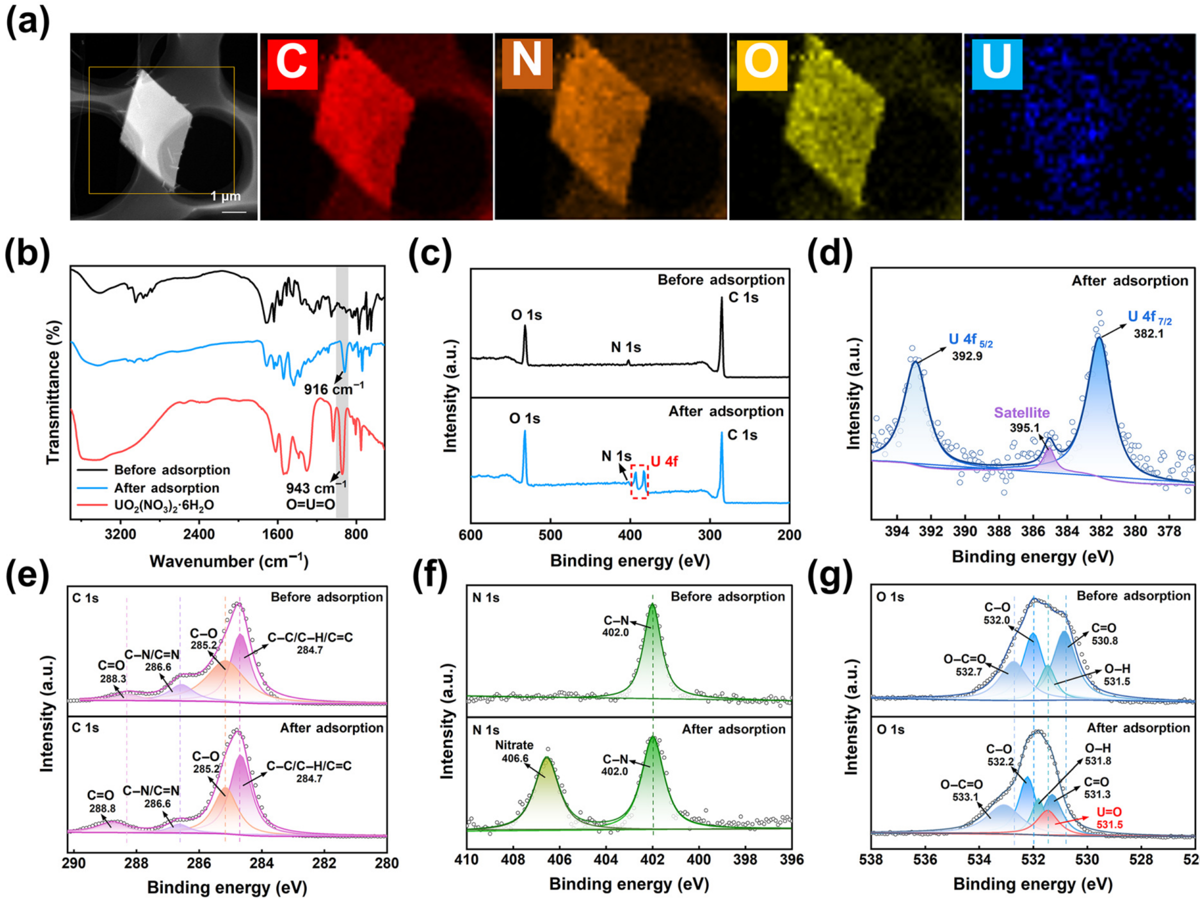

Figure 5 Characterization of U(VI) adsorption onto the BPTC-BPY-3. (a) Mapping diagram of BPTC-BPY-3 after adsorption of U(VI). (b) FT-IR spectra. (c) XPS full spectra and ((d)–(g)) XPS fine spectra of (d) U 4f, (e) C 1s, (f) N 1s, and (g) O 1s.

2.5 Adsorption mechanism of U(VI)

Next, the selective adsorption mechanism of U(VI) by BPTC-BPY-3 was systematically studied. Mapping revealed the homogeneous distribution of U(VI) on the adsorbent with other elements (including C, O, and N) from BPTC-BPY-3 (Fig. 5(a)). Complementary to this, energy dispersive spectroscopy (EDS) method was also carried out (Fig. S20 in the ESM). The content of uranium increased from a negligible presence to 24.1% upon adsorption of UO_2^{2+}. It was attributed to the higher binding capacity of the divalent UO_2^{2+} to the material. FT-IR and X-ray photoelectron spectroscopy (XPS) experiments of BPTC-BPY-3 loaded with UO_2^{2+} were carried out to elucidate the interaction between BPTC-BPY-3 and UO_2^{2+} at the molecular level. As shown in the FT-IR spectra (Fig. 5(b)), the characteristic antisymmetric stretching vibrational peak of O=U=O shifted from 932 to 916 cm^{-1} after adsorption, indicating that a strong interaction between UO_2^{2+} and BPTC-BPY-3 has been formed.

In addition, the appearance of the U 4f peak in the XPS spectra further confirmed the successful adsorption of U(VI) on BPTC-BPY-3 (Fig. 5(c)). The coordination behavior of UO_2^{2+} with BPTC-BPY-3 was further verified by showing the U 4f spectra of BPTC-BPY-3 after the adsorption of U(VI) in Fig. 5(d). The pristine peaks of U $4f_{5/2}$ and U $4f_{7/2}$ were located at 396.9 and 386.8 eV, respectively, with a spin-orbit splitting value of 10.1 eV [57]. In the case of BPTC-BPY-3 adsorption, new peaks with lower binding energies appeared for U $4f_{5/2}$ and U $4f_{7/2}$ at 392.9 and 382.1 eV, respectively, indicating that the U 4f binding energy peaks were shifted to lower binding energies. This implies that BPTC-BPY-3 closely interacts with UO_2^{2+}. The results demonstrate the occurrence of U ← O coordination reactions. For the C 1s spectra (Fig. 5(e)), prior to U(VI) adsorption, it can be decomposed into four independent peaks (284.7, 285.2, 286.6, and 288.3 eV) corresponding to C–C/C–H/C=C (carbon skeleton and phenyl group of the BPTC-BPY-3), C–O (carboxylate skeleton of the H_2BPTC^{2-}), C–N/C=N (BPY^{2+} pyridine ring), and C=O (carboxyl group). Upon adsorption of U(VI), the C 1s peak of C=O increased to 288.3 eV. This can be attributed to the fact that the O 1s peak of O–C=O increases to higher binding energies upon adsorption of uranium, and the carboxylate binding energies are characterized by a significant shift to higher energies, suggesting chelation with the uranyl cation. It can therefore be inferred that the carboxylate group of H_2BPTC^{2-} contributes significantly to the adsorption of uranium and that the electron cloud is tilted toward C due to binding with U(VI). As shown in the N 1s spectra (Fig. 5(f)), only one peak was observed at 402.0 eV in the original BPTC-BPY-3, which can be attributed to the C–N (pyridine ring of BPY^{2+}). After the adsorption of U(VI), a new peak with a binding energy of 406.6 eV appeared, which can be attributed to the nitrate from $UO_2(NO_3)_2{\cdot}6H_2O$. For the original O 1s spectra of BPTC-BPY-3 (Fig. 5(g)), the binding energies were categorized into four peaks corresponding to C=O (530.8 eV), O–H (531.5 eV), C–O (532.0 eV), and O–C=O (532.7 eV). After adsorption of U(VI), the overall shape of the O 1s peak changed significantly. A new peak belonging to the O=U=O group appeared at 531.5 eV, indicating the chemical interaction between BPTC-BPY-3 and U(VI). It is noteworthy that the binding energies of O–H and O–C=O increased to 531.8 and 533.1 eV, respectively, suggesting that the carboxyl group (O–C=O) plays important role in the adsorption of uranium through ligand and hydrogen bonding. In short, the C 1s, N 1s, and O 1s spectra strongly substantiate the binding of U(VI) to BPTC-BPY-3, predominantly through coordination of carboxyl functional groups on anionic biphenyls in BPTC-BPY-3. In addition, the presence of cation BPY^{2+} can adsorb anion (nitrate). Therefore, BPTC-BPY-3 has a remarkable adsorption capacity for U(VI) due to the coexistence of anions and cations, which can not only attract the U(VI) by electrostatic interactions, but also provide enough carboxyl groups.

U L_3-edge X-ray absorption near-edge structure (XANES) and extended X-ray absorption fine structure (EXAFS) were studied to detect the uranyl coordination environment in BPTC-BPY-3 after U(VI) adsorption. The typical characteristic peak at about 17,168 eV in the U L_3-edge XANES spectra was the so-called white line peak (Fig. 6(a)), which corresponds to the transition of electrons from the occupied U 2p state to the unoccupied 6d state. XANES spectra illustrated that BPTC-BPY-3 binds uranyl in the form of U(VI), and the collected data are very similar to the reference data of $U(VI)O_3$ and $U(VI)O_2(OH)_2$. Fourier transform of U L_3-edge EXAFS (Fig. 6(b)) showed that two peaks were detected at 1.79 and 2.34 Å in *R* space. Among them, the peak at 1.79 Å corresponds to the scattering path of axial oxygen atom ($U–O_{ax}$) in uranyl, and the peak at 2.34 Å corresponds to a coordination bond between uranium atom and carboxyl oxygen atom ($U–O_{eq}$) from carboxyl groups and coordinated water, which is consistent with the calculated coordination number between uranium and oxygen (Table S12 in the ESM).

To elucidate the adsorption mechanism and the detailed coordination structure at the BPTC-BPY-3 (solvent molecules are omitted) interface, the possible binding modes of U(VI) and V(V) with BPTC-BPY-3 were predicted by density functional theory (DFT) calculations, and the detailed interaction positions, binding energies, and selectivity mechanisms were obtained. The optimized configuration and adsorption energy of BPTC-BPY-3 on UO_2^{2+} and VO_3^- ligands are shown in Figs. 6(c) and 6(d). For BPTC-BPY-3, the predominant driving force of U(VI) adsorption comes from carboxyl groups in organic ligands. The coordination mode between carboxyl functional group and UO_2^{2+} (−4.85 eV) shows higher binding energy than that of VO_3^- (−2.54 eV). These results are basically consistent with the experimental data. Furthermore, the bond length between BPTC-BPY-3 and UO_2^{2+} (1.892 Å) is

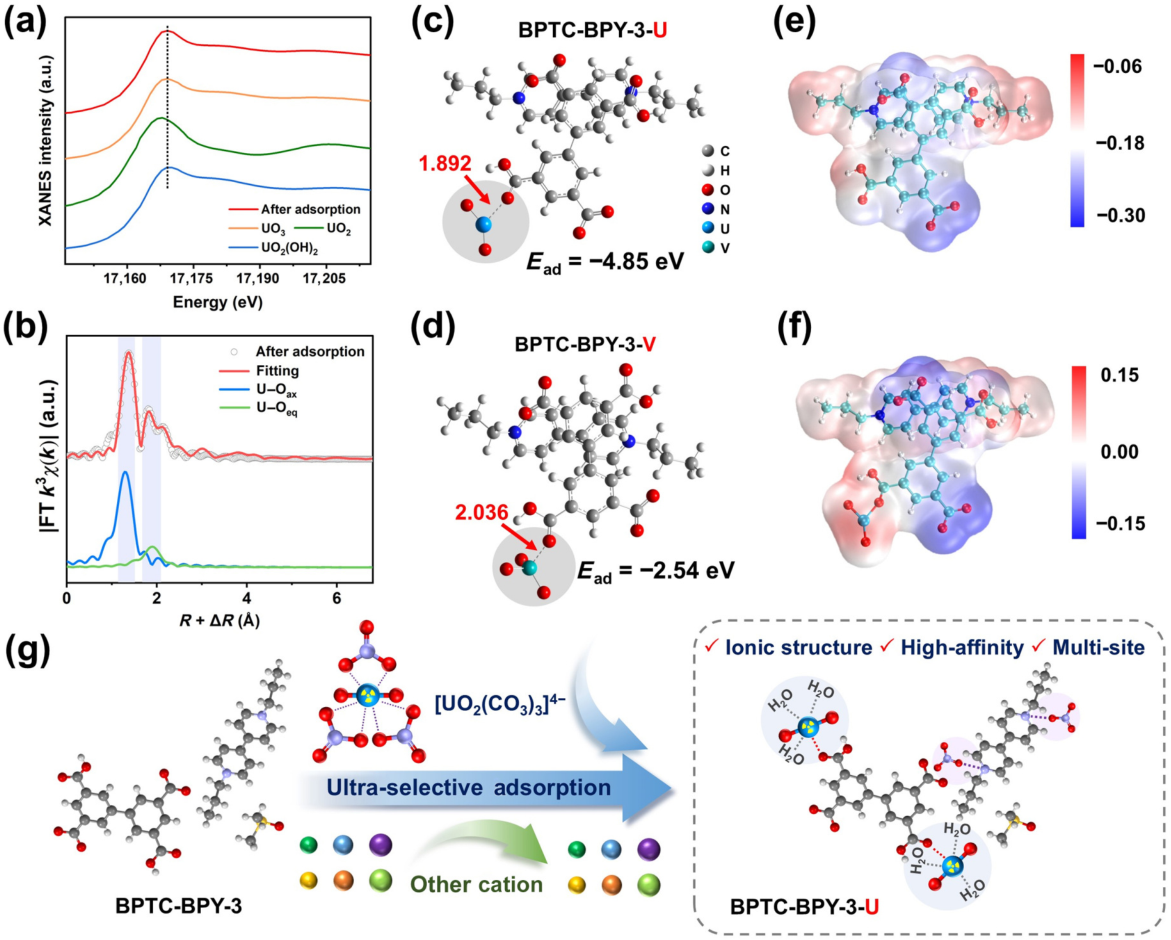

Figure 6 Adsorption mechanism of U(VI). (a) XANES spectra recorded at the U L_3-edge after adsorption of BPTC-BPY-3, and XANES data of the reference standards of UO_3, UO_2, and $UO_2(OH)_2$. (b) Corresponding k^3-weighted FT spectra. The blue line corresponds to the scattering path of axial oxygen atoms in uranyl and other oxygen atoms (such as oxygen atoms in uranyl-bound water). The green line corresponds to the coordination bond between uranium atom and oxygen atom from carboxylic acid group. ((c) and (d)) Optimized molecular structures of BPTC-BPY-3-U and BPTC-BPY-3-V. ((e) and (f)) Electrostatic potential diagrams of the optimized BPTC-BPY-3 and BPTC-BPY-3-U. (g) Mechanism of U(VI) adsorption by BPTC-BPY-3.

notably shorter than that of BPTC-BPY-3 and VO_3^- (2.036 Å), implying that the adsorption of uranyl ions on the single crystals is a chemisorption process, distinguished by superior selectivity. Electrostatic potential distribution calculations were then conducted to predict the chemical reaction propensity at each site, as shown in Figs. 6(e) and 6(f). Because the electrostatic attraction between molecules is intimately linked to the electrostatic interactions on the outer surface of the molecules during the initial stage of the chemical reaction. In the adsorption of U(VI) by BPTC-BPY-3, electrons were transferred from the uranyl ions to the single crystals, indicating significant covalent interactions between the single crystals and the uranyl ions.

Based on the above results, the adsorption mechanism of BPTC-BPY-3 on U(VI) can be described as follows: (1) coordination between uranium and carboxyl group of organic anion building block, and (2) the electrostatic interaction of the organic cation building block strengthens the adsorption of uranyl-coordinated anions (Fig. 6(g)). In addition, by tuning the length of alkyl chain, the stacking mode, specific surface area, and contact angle of the material were skillfully controlled, so that U(VI) could be effectively adsorbed on the ionic single crystal surface. These findings indicate that this adsorption material has great potential for application in uranium extraction from seawater.

3 Conclusions

In conclusion, utilizing viologen-derived with different alkyl chain lengths and polycarboxylic acid as organic ion building blocks, six ionic single crystals were firstly assembled, which were then employed as adsorbents in the development of UES through the synergistic effects of electrostatics and coordination exerted by the different organic ion building blocks. Among them, the higher specific surface area BPTC-BPY-3, based on its special stacking mode and more accessible sites, showed a quick ultra-selective adsorption of U(VI) with a maximum adsorption capacity of 686.8 mg/g within 2 min. In natural seawater, a satisfactory U(VI) uptake capacity of 7.41 mg/g was achieved in 20 days. The adsorption mechanism of uranyl ions analyzed by XPS, XAFS, and DFT calculations revealed that the special coordination ability of the carboxyl group endowed the adsorbent with high binding selectivity and binding affinity to U(VI), which effectively avoided the influence of interfering ions and achieved a high U(VI) extraction capacity in natural seawater. In addition, the adsorbent demonstrated exceptional stability and reusability, making it highly advantageous for practical applications for uranium extraction from seawater. This study demonstrated the significant tunability of electrostatic interactions in ionic materials through the utilization of anionic-cation building blocks, which may open new opportunities for the development of organic ionic single crystals formed by non-covalent interactions for other potential applications.

Electronic Supplementary Material: Supplementary material (materials, apparatus, materials preparation, adsorption performance tests for U(VI), and calculation method) is available in the online version of this article at https://doi.org/10.26599/NR.2025.94907856.

Data availability

All data needed to support the conclusions in the paper are presented in the manuscript and the Electronic Supplementary Material. Additional data related to this paper may be requested from the corresponding author upon request.

Acknowledgements

This work was supported by the National Natural Science Foundation of China (No. 22374159) and the Youth Innovation Promotion Association CAS (No. 2021420). We are grateful to the staff of Beijing Synchrotron Radiation Facility (BSRF) for EXAFS and XANES measurement.

Declaration of competing interest

All the contributing authors report no conflict of interests in this work.

Author contribution statement

J. H.: Conceptualization, methodology, writing – original draft, writing – review & editing, validation, formal analysis, investigation, resources, and data curation. J. C.: conceptualization, discussion, supervision, project administration, funding acquisition, writing – review & editing, validation. Y. X. S.: visualization and validation. Z. J. L.: investigation, visualization and validation. H. F. L.: visualization and validation. J. J. W.: visualization and validation. W. Q. S.: investigation, resources and supervision. H. D. Q.: conceptualization, supervision, discussion, writing – review & editing, validation. All the authors have approved the final manuscript.

Use of AI statement

None.

References

[1] Sholl, D. S.; Lively, R. P. Seven chemical separations to change the world. *Nature* **2016**, *532*, 435–437.

[2] Yuan, Y.; Cao, D. D.; Cui, F. C.; Yang, Y. J.; Zhang, C.; Song, Y. B.; Zheng, Y.; Cao, J. R.; Chen, S. S.; Song, Y. et al. High-capacity uranium extraction from seawater through constructing synergistic multiple dynamic bonds. *Nat. Water* **2025**, *3*, 89–98.

[3] Yu, K. F.; Zhou, L.; Wu, L. Z.; Dong, C. X.; Dong, H. H.; Lian, J.; Yang, X. Y.; Ahuja, R.; Chen, T.; Zhu, W. K. Photo-assisted uranium extraction based on heterogeneous catalysts. *Sci. Bull.* **2024**, *69*, 3800–3805.

[4] Chen, T.; Liu, T.; Zhou, L.; Li, M. X.; Meng, Q.; Yu, K. F.; Lian, J.; Zhu, W. K. Ternary boron carbon nitrides hollow nanotubes with tunable p–n homojunction for photo-assisted uranium extraction: A combined batch, EXAFS and DFT calculations. *Appl. Catal. B: Environ.* **2022**, *318*, 121815.

[5] Nan, Y.; Wang, J. L.; Chang, X.; Shao, K. J.; Lin, Y. C.; Qian, L. J.; Li, Z.; Hu, P. Z. Functionalized graphene oxide/sodium alginate beads with ion responsiveness for uranium trapping. *Carbohydr. Polym.* **2023**, *300*, 120259.

[6] Xu, M. Y.; Zhou, L.; Zhang, L. J.; Zhang, S. T.; Chen, F. L.; Zhou, R. H.; Hua, D. B. Two-dimensional imprinting strategy to create specific nanotrap for selective uranium adsorption with ultrahigh capacity. *ACS Appl. Mater. Interfaces* **2022**, *14*, 9408–9417.

[7] Yuan, Y. H.; Feng, S. W.; Feng, L. J.; Yu, Q. H.; Liu, T. T.; Wang, N. A bio-inspired nano-pocket spatial structure for targeting uranyl capture. *Angew. Chem., Int. Ed.* **2020**, *59*, 4262–4268.

[8] Yang, H.; Hao, M. J.; Xie, Y. H.; Liu, X. L.; Liu, Y. F.; Chen, Z. S.; Wang, X. K.; Waterhouse, G. I. N.; Ma, S. Q. Tuning local charge

distribution in multicomponent covalent organic frameworks for dramatically enhanced photocatalytic uranium extraction. *Angew. Chem., Int. Ed.* **2023**, *62*, e202303129.

[9] Song, Y. C.; Tan, H. H.; Qin, S. L.; Liu, Z.; Liu, C. T.; Shen, C. Y.; Yang, P. P.; Li, S. W. Assembly of a core–shell MOF with stability into polyacrylamide hydrogel for boosting extraction of uranium from seawater. *Nano Res.* **2024**, *17*, 3398–3406.

[10] Wang, J. Y.; Zhou, W. Q.; Shi, Y. L.; Li, Y.; Xian, D. F.; Guo, N.; Liu, C. L. Uranium sorption on oxyhydroxide minerals by surface complexation and precipitation. *Chin. Chem. Lett.* **2022**, *33*, 3461–3467.

[11] Cui, A. Q.; Wu, X. Y.; Ye, J. B.; Song, G.; Chen, D. Y.; Xu, J.; Liu, Y.; Lai, J. P.; Sun, H. "Two-in-one" dual-function luminescent MOF hydrogel for onsite ultra-sensitive detection and efficient enrichment of radioactive uranium in water. *J. Hazard. Mater.* **2023**, *448*, 130864.

[12] Cui, W. R.; Zhang, C. R.; Xu, R. H.; Chen, X. R.; Jiang, W.; Li, Y. J.; Liang, R. P.; Zhang, L.; Qiu, J. D. Rational design of covalent organic frameworks as a groundbreaking uranium capture platform through three synergistic mechanisms. *Appl. Catal. B: Environ.* **2021**, *294*, 120250.

[13] Liu, T. Q.; Li, Z.; Zhang, X.; Tan, H. X.; Chen, Z. Y.; Wu, J. S.; Chen, J.; Qiu, H. D. Metal–organic framework-intercalated graphene oxide membranes for selective separation of uranium. *Anal. Chem.* **2021**, *93*, 16175–16183.

[14] Wang, D.; Song, J. N.; Wen, J.; Yuan, Y. H.; Liu, Z. L.; Lin, S.; Wang, H. Y.; Wang, H. L.; Zhao, S. L.; Zhao, X. M. et al. Significantly enhanced uranium extraction from seawater with mass produced fully amidoximated nanofiber adsorbent. *Adv. Energy Mater.* **2018**, *8*, 1802607.

[15] Yang, S.; Cao, Y.; Wang, T.; Cai, S. Y.; Xu, M. Y.; Lu, W. H.; Hua, D. B. Positively charged conjugated microporous polymers with antibiofouling activity for ultrafast and highly selective uranium extraction from seawater. *Environ. Res.* **2020**, *183*, 109214.

[16] Yuan, Y. H.; Yu, Q. H.; Wen, J.; Li, C. Y.; Guo, Z. H.; Wang, X. L.; Wang, N. Ultrafast and highly selective uranium extraction from seawater by hydrogel-like spidroin-based protein fiber. *Angew. Chem., Int. Ed.* **2019**, *58*, 11785–11790.

[17] Zhang, Y.; Huang, S. Q.; Mei, B. Y.; Jia, L. Y.; Liao, J.; Zhu, W. K. Construction of dopamine supported Mg(Ca)Al layered double hydroxides with enhanced adsorption properties for uranium. *Sci. Total Environ.* **2023**, *881*, 163525.

[18] Feng, L. J.; Wang, H.; Feng, T. T.; Yan, B. J.; Yu, Q. H.; Zhang, J. C.; Guo, Z. H.; Yuan, Y. H.; Ma, C. X.; Liu, T. et al. *In situ* synthesis of uranyl-imprinted nanocage for selective uranium recovery from seawater. *Angew. Chem. , Int. Ed.* **2022**, *61*, e202101015.

[19] Zhao, S. L.; Yuan, Y. H.; Yu, Q. H.; Niu, B. Y.; Liao, J. H.; Guo, Z. H.; Wang, N. A dual-surface amidoximated halloysite nanotube for high-efficiency economical uranium extraction from seawater. *Angew. Chem., Int. Ed.* **2019**, *58*, 14979–14985.

[20] Zhang, W. H.; Xu, C. L.; Che, X. P.; Wang, T.; Willför, S.; Li, M. J.; Li, C. X. Encapsulating amidoximated nanofibrous aerogels within wood cell tracheids for efficient cascading adsorption of uranium ions. *ACS Nano* **2022**, *16*, 13144–13151.

[21] Yu, Q. H.; Yuan, Y. H.; Feng, L. J.; Feng, T. T.; Sun, W. Y.; Wang, N. Spidroin-inspired, high-strength, loofah-shaped protein fiber for capturing uranium from seawater. *Angew. Chem., Int. Ed.* **2020**, *59*, 15997–16001.

[22] Li, X.; Liu, Z. R.; Huang, M. Purification of uranium-containing wastewater by adsorption: A review of research on resin materials. *J. Radioanal. Nucl. Chem.* **2022**, *331*, 3043–3075.

[23] Yan, B. J.; Ma, C. X.; Gao, J. X.; Yuan, Y. H.; Wang, N. An ion-crosslinked supramolecular hydrogel for ultrahigh and fast uranium recovery from seawater. *Adv. Mater.* **2020**, *32*, 1906615.

[24] Liang, H. X.; Mu, Y. L.; Yin, M. Y.; He, P. P.; Guo, W. W. Solar-powered simultaneous highly efficient seawater desalination and highly specific target extraction with smart DNA hydrogels. *Sci. Adv.* **2023**, *9*, eadj1677.

[25] Yang, J. J.; Geng, N. B.; Li, Y.; Wu, L. D.; Chang, T.; Shi, H. T.; Ahmad, Z.; Jiang, M. J.; Qu, J.; Zhang, H. J. et al. Wax-casted macroporous polyamidoxime hydrogel particles encapsulated in alginate-polyacrylic acid beads for highly efficient uranium capture from seawater. *Adv. Funct. Mater.* **2024**, *35*, 2418340.

[26] Ma, Y.; Liu, L.; Zhao, S. L.; Xu, X. Z.; Wang, Y.; Zhang, Y. L.; Rong, H. Z.; Yuan, Y. H.; Wang, N. Molecular engineering of multivariate porous aromatic frameworks for recovery of dispersed uranium resources. *Adv. Funct. Mater.* **2024**, *34*, 2410778.

[27] Ma, C. X.; Gao, J. X.; Wang, D.; Yuan, Y. H.; Wen, J.; Yan, B. J.; Zhao, S. L.; Zhao, X. M.; Sun, Y.; Wang, X. L. et al. Sunlight polymerization of poly(amidoxime) hydrogel membrane for enhanced uranium extraction from seawater. *Adv. Sci.* **2019**, *6*, 1900085.

[28] Xie, Y.; Liu, Z. Y.; Geng, Y. Y.; Li, H.; Wang, N.; Song, Y. P.; Wang, X. L.; Chen, J.; Wang, J. C.; Ma, S. Q. et al. Uranium extraction from seawater: Material design, emerging technologies and marine engineering. *Chem. Soc. Rev.* **2023**, *52*, 97–162.

[29] Zhang, L.; Luo, Y. T.; Xiao, S. J.; Fan, J. Q.; Tan, Q. G.; Sun, C.; Song, A. M.; Liang, R. P.; Qiu, J. D. The construction of a stable hydrogen-bonded organic framework for the photocatalytic reduction and removal of uranium. *Chem. Commun.* **2024**, *60*, 3583–3586.

[30] Huang, Z. W.; Li, X. B.; Mei, L.; Han, Y. Z.; Song, Y. T.; Fu, X.; Zhang, Z. H.; Guo, Z. J.; Zeng, J. R.; Bian, F. G. et al. All-in-one: Photo-responsive lanthanide–organic framework for simultaneous sensing, adsorption, and photocatalytic reduction of uranium. *Adv. Funct. Mater.* **2024**, *34*, 2404126.

[31] More, Y. D.; Mollick, S.; Saurabh, S.; Fajal, S.; Tricarico, M.; Dutta, S.; Shirolkar, M. M.; Mandal, W.; Tan, J. C.; Ghosh, S. K. Nanotrap grafted anionic MOF for superior uranium extraction from seawater. *Small* **2024**, *20*, 2302014.

[32] Pan, J. M.; Xiao, B. T.; Zhu, W.; Yang, Y. N.; Huang, H. L.; Lian, Z. C.; Zhang, T.; Qiu, F. X.; Xue, S. L.; Pang, H. Photocatalytic uranium extraction boosted by dual effective active sites of porphyrin metal–organic frameworks. *Nano Res.* **2024**, *17*, 6713–6720.

[33] Wang, X. J.; Reischauer, S.; Xie, H. M.; Han, G. H.; Wellman, H.; Kirlikovali, K. O.; Idrees, K.; Son, F. A.; Notestein, J. M.; Farha, O. K. Advancements in cerium/titanium metal–organic frameworks: Unparalleled stability in CO oxidation. *Matter* **2024**, *7*, 3845–3856.

[34] Li, B.; Cheng, Y. Z.; Ma, X. Y.; Zhao, D. X.; Zhang, Y.; Sun, Y. X.; Chen, J.; Wu, L.; Zhao, L.; Qiu, H. D. et al. Facile and scale-up synthesis of cyano-functionalized covalent organic frameworks for selective gold recovery. *Chin. Chem. Lett.*, in press, DOI: 10.1016/j.cclet.2025.111134.

[35] Lin, T.; Chen, T.; Jiao, C.; Zhang, H. Y.; Hou, K.; Jin, H. X.; Liu, Y.; Zhu, W. K.; He, R. Ion pair sites for efficient electrochemical extraction of uranium in real nuclear wastewater. *Nat. Commun.* **2024**, *15*, 4149.

[36] Li, J.; Xie, R. Z.; Li, B. Y.; Chen, L. X.; Shen, W. H.; Zhao, Y. T.; Guo, Q.; Chen, L.; Xu, B. Q.; Chen, X. J. et al. Tumor imaging by a $^{99m}TcO_4^-$-labeled cationic polymeric network. *CCS Chem.* **2024**, *6*, 1868–1875.

[37] Wang, L. Y.; Yu, J. J.; Wang, S.; Liu, Y.; Song, K. X.; Yu, J. P.; Yuan, L. Y.; Liu, Z. R.; Shi, W. Q. Pyridine-based ionic sp^2 carbon-conjugated covalent organic frameworks for selective extraction of Pu(IV) from high-level liquid waste. *Chin. Chem. Lett.* **2024**, *36*, 110706.

[38] Liu, H. F.; He, Y. R.; Chen, J.; Qu, X. Q.; He, J.; Chen, X. W.; Wang, J. H.; Qiu, H. D. Chiral ionic organic single-crystal and its exfoliated two-dimensional nanosheets with enhanced enantioseparation. *Chem. Sci.* **2024**, *15*, 18818–18824.

[39] Guo, J.; Zhang, Y.; Zhu, Y. F.; Long, C.; Zhao, M. T.; He, M.; Zhang, X. F.; Lv, J. W.; Han, B.; Tang, Z. Y. Ultrathin chiral metal–organic-framework nanosheets for efficient enantioselective separation. *Angew. Chem., Int. Ed.* **2018**, *57*, 6873–6877.

[40] Park, K. C.; Martin, C. R.; Leith, G. A.; Thaggard, G. C.; Wilson, G. R.; Yarbrough, B. J.; Maldeni Kankanamalage, B. K. P.; Kittikhunnatham, P.; Mathur, A.; Jatoi, I. et al. Capture instead of

release: Defect-modulated radionuclide leaching kinetics in metal–organic frameworks. *J. Am. Chem. Soc.* **2022**, *144*, 16139–16149.

[41] Zhang, P.; Chen, Y. W.; Chen, Y. Z.; Guo, Q. Q.; Liu, Y. S.; Yang, Y.; Cao, Q.; Chong, H. B.; Lin, M. Z. Functionalized hierarchically porous carbon doped boron nitride for multipurpose and efficient treatment of radioactive sewage. *Sci. Total Environ.* **2023**, *866*, 161378.

[42] Gao, Y. Y.; Zhang, Q.; Lv, Y.; Wang, S.; Men, M.; Kobayashi, H.; Xu, Z. L.; Wang, Y. Peptide-carbon hybrid membranes for highly efficient and selective extraction of actinides from rare earth elements. *J. Mater. Chem. A* **2021**, *9*, 14422–14431.

[43] Li, H.; Sun, J.; Qin, S. L.; Song, Y. C.; Liu, Z.; Yang, P. P.; Li, S. W.; Liu, C. T.; Shen, C. Y. Zwitterion functionalized graphene oxide/polyacrylamide/polyacrylic acid hydrogels with photothermal conversion and antibacterial properties for highly efficient uranium extraction from seawater. *Adv. Funct. Mater.* **2023**, *33*, 2301773.

[44] Kaushik, A.; Marvaniya, K.; Kulkarni, Y.; Bhatt, D.; Bhatt, J.; Mane, M.; Suresh, E.; Tothadi, S.; Patel, K.; Kushwaha, S. Large-area self-standing thin film of porous hydrogen-bonded organic framework for efficient uranium extraction from seawater. *Chem* **2022**, *8*, 2749–2765.

[45] Song, Y. C.; Ma, X.; Tan, H. H.; Liu, Z.; Liu, C. T.; Shen, C. Y.; Yang, P. P.; Li, S. W. Hollow Zn/Co zeolitic imidazolate framework-implanted composite hydrogel for highly efficient uranium extraction from seawater. *Nano Res.* **2023**, *16*, 10451–10461.

[46] Yuan, Y. H.; Yu, Q. H.; Cao, M.; Feng, L. J.; Feng, S. W.; Liu, T. T.; Feng, T. T.; Yan, B. J.; Guo, Z. H.; Wang, N. Selective extraction of uranium from seawater with biofouling-resistant polymeric peptide. *Nat. Sustain.* **2021**, *4*, 708–714.

[47] Yuan, Y. H.; Niu, B. Y.; Yu, Q. H.; Guo, X.; Guo, Z. H.; Wen, J.; Liu, T.; Zhang, H. Q.; Wang, N. Photoinduced multiple effects to enhance uranium extraction from natural seawater by black phosphorus nanosheets. *Angew. Chem., Int. Ed.* **2020**, *59*, 1220–1227.

[48] Xu, X.; Zhang, H. J.; Ao, J. X.; Xu, L.; Liu, X. Y.; Guo, X. J.; Li, J. Y.; Zhang, L.; Li, Q. N.; Zhao, X. Y. et al. 3D hierarchical porous amidoxime fibers speed up uranium extraction from seawater. *Energy Environ. Sci.* **2019**, *12*, 1979–1988.

[49] Hao, M. J.; Xie, Y. H.; Liu, X. L.; Chen, Z. S.; Yang, H.; Waterhouse, G. I. N.; Ma, S. Q.; Wang, X. K. Modulating uranium extraction performance of multivariate covalent organic frameworks through donor–acceptor linkers and amidoxime nanotraps. *JACS Au* **2023**, *3*, 239–251.

[50] Wu, Y. D.; Cui, W. R.; Zhang, C. R.; Liang, R. P.; Qiu, J. D. Regenerable, anti-biofouling covalent organic frameworks for monitoring and extraction of uranium from seawater. *Environ. Chem. Lett.* **2021**, *19*, 1847–1856.

[51] Shi, S.; Qian, Y. X.; Mei, P. P.; Yuan, Y. H.; Jia, N.; Dong, M. Y.; Fan, J. C.; Guo, Z. H.; Wang, N. Robust flexible poly(amidoxime) porous network membranes for highly efficient uranium extraction from seawater. *Nano Energy* **2020**, *71*, 104629.

[52] Zhao, L.; Wang, S. Y.; Wang, G.; Cai, L. R.; Sun, L. N.; Qiu, J. S. Phosphorus nitride imide nanotubes for uranium capture from seawater. *ACS Nano* **2024**, *18*, 11804–11812.

[53] Yu, R.; Zhang, X. S.; Lu, Y. R.; Chen, W.; Chen, X.; Li, L. B. Advanced amidoximated polyethylene nanofibrous membranes for practical uranium extraction from seawater. *ACS Sustain. Chem. Eng.* **2022**, *10*, 12307–12318.

[54] Liang, C. Y.; Tuo, K.; Hou, W. F.; Li, Y.; Shao, C. C.; Sun, Y. X.; Xu, W.; Cao, S. Y.; Zhang, D. B.; Pu, S. Z. et al. Construction of a core–shell–shell structured superparamagnetic amidoxime functionalized metal–organic framework for uranium extraction from seawater. *J. Water Process Eng.* **2025**, *72*, 107586.

[55] Zhou, W.; Li, A. M.; Zhou, M.; Xu, Y. Y.; Zhang, Y.; He, Q. Nonporous amorphous superadsorbents for highly effective and selective adsorption of iodine in water. *Nat. Commun.* **2023**, *14*, 5388.

[56] Li, X.; Liu, Q.; Chen, S. S.; Zhu, J. H.; Song, Y.; Wu, H. T.; Li, Y.; Chen, R. R.; Yu, J.; Liu, J. Y. et al. Anti-biofouling amidoxime-quaternized polyethyleneimine hemp fiber for efficient uranium extraction from seawater. *Chem. Eng. J.* **2024**, *497*, 154563.

[57] Mollick, S.; Saurabh, S.; More, Y. D.; Fajal, S.; Shirolkar, M. M.; Mandal, W.; Ghosh, S. K. Benchmark uranium extraction from seawater using an ionic macroporous metal–organic framework. *Energy Environ. Sci.* **2022**, *15*, 3462–3469.